Article

Quantum register of fermion pairs

https://doi.org/10.1038/s41586-021-04205-8

Received: 23 March 2021

Accepted: 3 November 2021

Thomas Hartke[1]✉, Botond Oreg[1], Ningyuan Jia[1] & Martin Zwierlein[1]✉

Quantum control of motion is central for modern atomic clocks[1] and interferometers[2]. It enables protocols to process and distribute quantum information[3,4], and allows the probing of entanglement in correlated states of matter[5]. However, the motional coherence of individual particles can be fragile to maintain, as external degrees of freedom couple strongly to the environment. Systems in nature with robust motional coherence instead often involve pairs of particles, from the electrons in helium, to atom pairs[6], molecules[7] and Cooper pairs. Here we demonstrate long-lived motional coherence and entanglement of pairs of fermionic atoms in an optical lattice array. The common and relative motion of each pair realize a robust qubit, protected by exchange symmetry. The energy difference between the two motional states is set by the atomic recoil energy, is dependent on only the mass and the lattice wavelength, and is insensitive to the noise of the confining potential. We observe quantum coherence beyond ten seconds. Modulation of the interactions between the atoms provides universal control of the motional qubit. The methods presented here will enable coherently programmable quantum simulators of many-fermion systems[8], precision metrology based on atom pairs and molecules[9,10] and, by implementing further advances[11–13], digital quantum computation using fermion pairs[14].

The Pauli principle lends stability to matter, from the shell structure of nuclei and the periodic system of elements to Pauli pressure protecting a neutron star from gravitational collapse. In search of robust coherence in many-body quantum mechanical systems, one may strive to emulate the particular stability of noble gases and magic nuclei, provided by fully filled shells of fermions. Interactions between fermions can further enhance stability, for example, via the formation of Cooper pairs in nuclear matter and superconductors, which opens energy gaps and thereby creates protected subspaces for fermion pairs. Thus fermion anti-symmetry and strong interactions, the core challenges for classical computations of many-fermion behaviour[15], may offer decisive solutions for protecting and processing quantum information.

Recent advances in quantum gas microscopy[8,11] have enabled analogue quantum simulations of fermionic systems at the resolution of individual atoms. These platforms thus offer clear prospects towards coherent control utilizing fermionic hardware.

Here we create and control an array of fermion pairs featuring long-lived vibrational coherence, and demonstrate its potential for robust encoding and manipulation of quantum information. Starting with a many-fermion system in a Hubbard-regime optical lattice, we leverage fermionic statistics to initialize[16–18] a low-entropy array of spin-singlet fermion pairs, and to restrict the fermion dynamics to a symmetry-protected subspace. Quantum information is encoded in the motional state[19–23] of the atom pair by forming superpositions of the centre-of-mass (COM) and relative vibrational motion. Working in a subspace of pairs of atoms decouples the quantum information from environmental noise[14,24,25]. Strong interactions are induced via a Feshbach resonance[26–29], allowing for tunability of the two-fermion motional qubit frequency over several orders of magnitude.

To initialize the quantum register, we cool a two-state mixture of fermionic neutral ^{40}K atoms into the lowest band of a two-dimensional (2D) optical lattice. Increasing the lattice potential creates a large array of hundreds of fermion pairs in isolated wells, with each fermion occupying the three-dimensional (3D) motional ground state of its well (Fig. 1a). Pauli exclusion is crucial in this preparation step: it energetically freezes out triply occupied sites and it forces the spin wavefunction of each fermion pair to be a spin singlet, thereby protecting the two-particle spatial wavefunction $\Psi(\mathbf{r}_1, \mathbf{r}_2)$ to remain symmetric under exchange of the atomic positions $\mathbf{r}_1$ and $\mathbf{r}_2$ at all times, $\Psi(\mathbf{r}_1, \mathbf{r}_2) = \Psi(\mathbf{r}_2, \mathbf{r}_1)$. Motion in each well occurs in the quasi-one-dimensional (1D) regime, with in-plane (x–y) confinement much stronger than in the out-of-plane (z) direction (angular frequencies $\omega_{x,y} \approx 4\omega_z$). The quantum information is encoded in the subspace of vibrational states with two units of harmonic energy along z ($2\hbar\omega_z$, with $\hbar$ *the reduced Planck constant)*, where exactly two symmetric two-particle states exist. In the first state $|1, 1\rangle$, each atom carries one excitation, whereas in the second state $|0, 2\rangle_s = (|0, 2\rangle + |2, 0\rangle)/\sqrt{2}$, one atom carries both quanta, leaving the other in the ground state. These two states differ in only how vibration is distributed within the atom pair, and are thus immune to fluctuations in $\hbar\omega_z$. In general, single-particle perturbations can only couple the pair states at second order. As the singlet spin wavefunction is a bystander to the pair motion, pairs are also immune against magnetic field noise.

To access this symmetry-protected subspace, we make use of a Feshbach resonance[26] caused by an avoided crossing of the atom pair with a molecular state (Fig. 1b). Sweeping the magnetic field across the resonance injects $2\hbar\omega_z$ energy into the relative motion of the fermion pair[27–29] promoting it to the state $|2\rangle_{\rm rel}$, while leaving the COM motion in the harmonic ground state, $|0\rangle_{\rm COM}$. At the magnetic field B_0 where

---

[1]Department of Physics, MIT-Harvard Center for Ultracold Atoms, Research Laboratory of Electronics, MIT, Cambridge, MA, USA. ✉e-mail: hartke@mit.edu; zwierlein@mit.edu

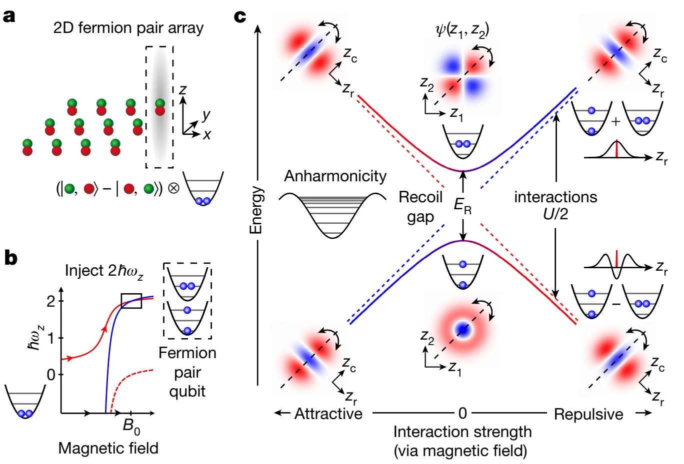

Fig. 1 | Spatial qubit encoding in a pair of entangled fermions. a, An array of fermion pairs prepared from a two-component, fermionic quantum gas in an optical lattice. Each lattice site (dashed box) initially contains two fermionic atoms in the spatial ground state of a 3D anisotropic harmonic trap, forming a spin singlet. Information is stored in the spatial wavefunction in the z direction, which must remain exchange symmetric $\Psi(z_1, z_2) = \Psi(z_2, z_1)$ (blue spheres). **b**, Injection of $2\hbar\omega_z$ vibrational energy via a magnetic field sweep across a Feshbach resonance with a molecular state (red dashed line) brings the fermion pair (red solid line) to the qubit subspace. For vanishing interatomic interactions, at field B_0, there are two degenerate two-particle states of harmonic motion along z, with atoms either both in the first excited state $|1, 1\rangle$ or with one atom carrying two excitations $|0, 2\rangle_s$ (dashed box). The latter state is adiabatically connected to a molecular state in COM motion (blue line). **c**, Full control over the fermion pair qubit via trap anharmonicity and tunable interatomic interactions. At vanishing interactions (centre), anharmonicity nonlinearly reduces the energy of excited harmonic states (left schematic). States $|1, 1\rangle$ (upper box) and $|0, 2\rangle_s$ (lower box) are split by the recoil energy $E_R = \hbar^2\pi^2/(2ma_z^2)$, determined solely by geometry (lattice spacing a_z) and the atomic mass m. Strong interactions ($|U| \gg E_R$, left and right side) fully mix the anharmonic eigenstates. The fermion pair stores the $2\hbar\omega_z$ vibrational energy in either COM motion $z_c = (z_1 + z_2)/\sqrt{2}$ (upper right box) or relative motion $z_r = (z_1 - z_2)/\sqrt{2}$ (lower right box). This avoided crossing enables universal control of fermion pair qubits.

interactions vanish, this atom pair in relative motion becomes degenerate with the state $|2\rangle_{\mathrm{COM}}|0\rangle_{\mathrm{rel}}$ where the two atoms instead have two units of COM motion[30,31]. The latter emerges from a molecular state with that same excited COM motion existing at $B < B_0$.

Control of the fermion pair qubit is achieved via tunable interactions and the anharmonicity of the lattice potential, which couples the interacting states[32–35]. Figure 1c shows a schematic of the energy spectrum and two-particle spatial wavefunctions $\Psi(z_1, z_2)$ of the fermion pair qubit states as interactions are tuned from attractive to vanishing to repulsive using the magnetic field. For each fermion pair state, $\Psi(z_1, z_2)$ is reflection symmetric about the line $z_1 = z_2$.

At vanishing interactions, the degeneracy of the two pair qubit states is lifted by the anharmonicity of the lattice (centre of Fig. 1c). Each atom experiences an identical periodic potential $VE_R\sin(\pi z/a_z)^2$, where the lattice depth V is given in units of the recoil energy $E_R = \hbar^2\pi^2/(2ma_z^2)$, with m the atomic mass and a_z the lattice periodicity. For $V \gg 1$ (in the experiment, $V \approx 8{,}000$), atoms experience a deep lattice and are localized near the potential minima. To first order, the trap is harmonic with

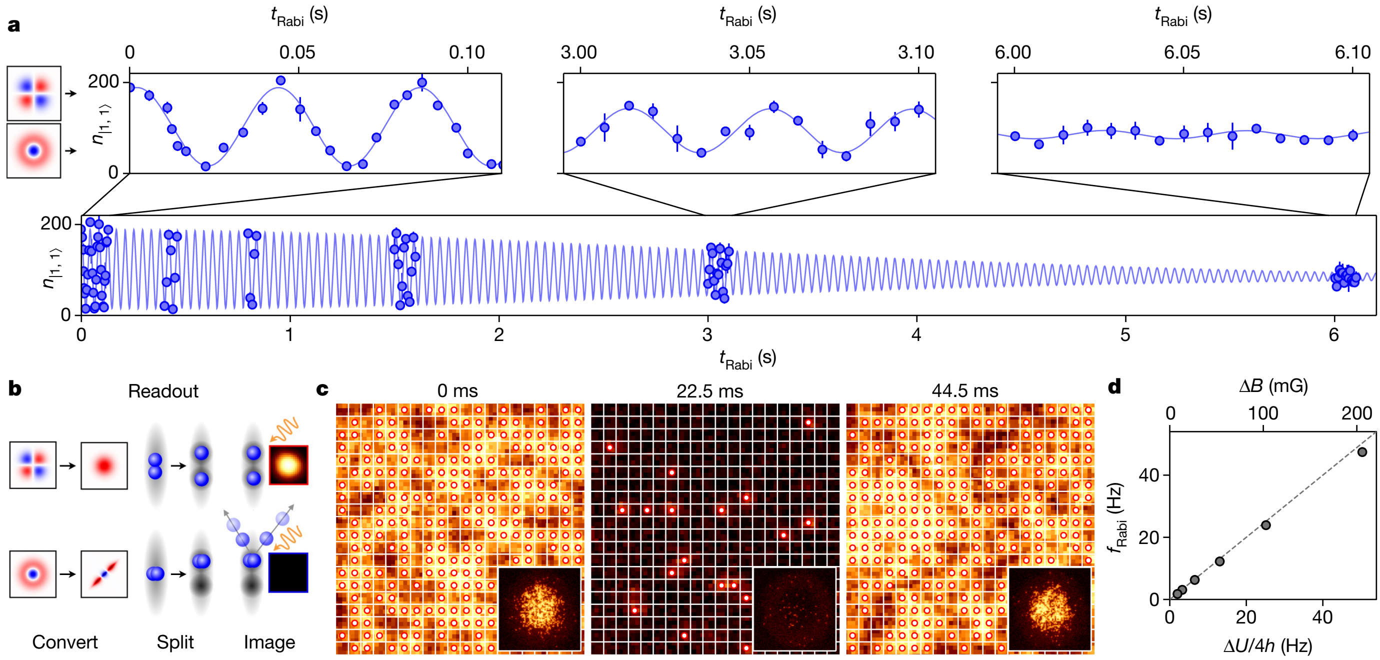

Fig. 2 | Simultaneous coherent manipulation and parallel readout of hundreds of motional fermion pair qubits. a, Modulation of interactions at the recoil gap drives a Rabi oscillation between fermion pair states $|1, 1\rangle$ and $|0, 2\rangle_s$, measured via the number $n_{|1,1\rangle}$ of pairs in state $|1, 1\rangle$ in a central region of the 2D array (Methods). **b**, Readout proceeds by converting each fermion pair to either a molecule (lower panel) or repulsive pair (upper panel) using the Feshbach resonance. Application of a superlattice then splits repulsive pairs into their fermionic constituents for fluorescence imaging, whereas tightly bound molecules are ejected and appear dark[37]. **c**, A single fluorescence image reveals each of the fermion pair qubits in parallel, with single-site resolution. The field of view displayed is 20 × 20 lattice sites, with the lower right insets showing the entire atomic cloud. **d**, Measured Rabi frequency f_{Rabi} versus the measured magnetic field modulation ΔB, and corresponding calculated interaction energy modulation $\Delta U/4$. The dashed line shows the predicted Rabi frequency $f_{\mathrm{Rabi}} = \Delta U/4h$, in good agreement with experiment. Here, and elsewhere, error bars on $n_{|1,1\rangle}$ show the standard deviation from two or three repetitions. Error bars representing the fit error for f_{Rabi} are smaller than the datapoints.

energy $\hbar\omega_z = 2E_{\rm R}\sqrt{V}$, and the pair states $|1,1\rangle$ and $|0,2\rangle_{\rm s}$ are degenerate, removing dependence of their energy difference on V. At second order, the quartic corrections proportional to $VE_{\rm R}(z/a_z)^4$ have two crucial effects. First, the characteristic size of the wavepacket scales with the harmonic oscillator length $\sqrt{\hbar/m\omega_z} = (a_z/\pi)V^{-1/4}$, leading to quartic corrections on the scale of the recoil energy $E_{\rm R}$, independent of the potential depth. Second, because $\langle n|z^4|n\rangle$ grows as n^2 for states with n excitations, the single-particle energy spectrum becomes nonlinear $E_n - E_0 \approx n\hbar\omega_z - n(n+1)E_{\rm R}/2$, which breaks the degeneracy of the atom pair states. As a result, $|0,2\rangle_{\rm s}$ shifts below $|1,1\rangle$ by $E_{\rm R}$, which we call the recoil gap. The relative fluctuations of this gap with V, due to the next-order (Methods) corrections $(9/8)E_{\rm R}/\sqrt{V}$, are strongly suppressed by $\sqrt{V} \gg 1$, highlighting the advantages of atom-pair states compared with encoding information in single-particle harmonic states[19–23]. Moreover, the existence and inherent stability of the recoil gap are not specific to a lattice potential, and are a general feature of any anharmonic potential with rigid shape, with the role of a_z replaced by another geometric scale.

When repulsive interactions dominate (right side of Fig. 1c), the fermion pair behaves like two pendula coupled by a spring, and the atoms oscillate with two quanta in either common or relative motion. Indeed, the higher-energy pair state, when viewed along the COM and relative axes, is simply $|2\rangle_{\rm COM}|0\rangle_{\rm rel} = (|0,2\rangle_{\rm s} + |1,1\rangle)/\sqrt{2}$, whereas the lower-energy state is $|0\rangle_{\rm COM}|2\rangle_{\rm rel} = (|0,2\rangle_{\rm s} - |1,1\rangle)/\sqrt{2}$. In the relative ground state $|0\rangle_{\rm rel}$, atoms overlap maximally and experience a repulsive energy shift $U \equiv {}_{\rm rel}\langle 0|\hat{U}|0\rangle_{\rm rel}$ from two-particle interactions $\hat{U}$, whereas in $|2\rangle_{\rm rel}$ they less strongly overlap, leading to a weaker shift (Methods) ${}_{\rm rel}\langle 2|\hat{U}|2\rangle_{\rm rel} = U/2$. The resulting energy separation between the pair states is $U/2$, which is set by the interaction strength and is experimentally controlled via the magnetic field.

In Fig. 2a, we demonstrate universal control of the fermion pair qubit by driving a Rabi oscillation between the recoil gap eigenstates $|1,1\rangle$ and $|0,2\rangle_{\rm s}$. Analogous to any two-level system, Rabi oscillations are produced by modulating an off-diagonal matrix element, the interaction energy $\langle 1,1|\hat{U}|0,2\rangle_{\rm s} = U/4$, at the frequency of the recoil gap[36] (Methods). The oscillation is observed by counting the number $n_{|1,1\rangle}$ of fermion pairs in state $|1,1\rangle$ in a central region of the 2D array (Methods). To detect the state of each pair qubit, we engineer state $|1,1\rangle$ to fluoresce when imaged, and state $|0,2\rangle_{\rm s}$ to appear dark (Fig. 2b). This is achieved by coherently splitting exclusively fermion pairs in $|1,1\rangle$ via a double well into two separate, spin-entangled fermions, which are subsequently imaged. With a single image of separated atom pairs under a quantum gas microscope[37], parallel readout of all fermion pair qubits in the 2D array is achieved with single-site resolution. Figure 2c shows the first complete Rabi cycle, as the 2D register array Rabi oscillates from $|1,1\rangle$ (bright) to $|0,2\rangle_{\rm s}$ (dark) and returns to $|1,1\rangle$.

The measured Rabi frequency $f_{\rm Rabi}$ of the interaction-driven pair qubit agrees well, for moderate driving, with the interaction modulation $\Delta U/4$, calculated from the calibrated trap parameters and scattering properties (Methods, Fig. 2d). The robust energy separation between the pair qubit states and other symmetry-protected states of the fermion pair allows increasing the Rabi coupling to values at and beyond the recoil gap. In this non-perturbative regime of strong driving, the fermion pair exhibits a non-sinusoidal response (Methods), which can be used for quantum control at rates exceeding the energy gap[38].

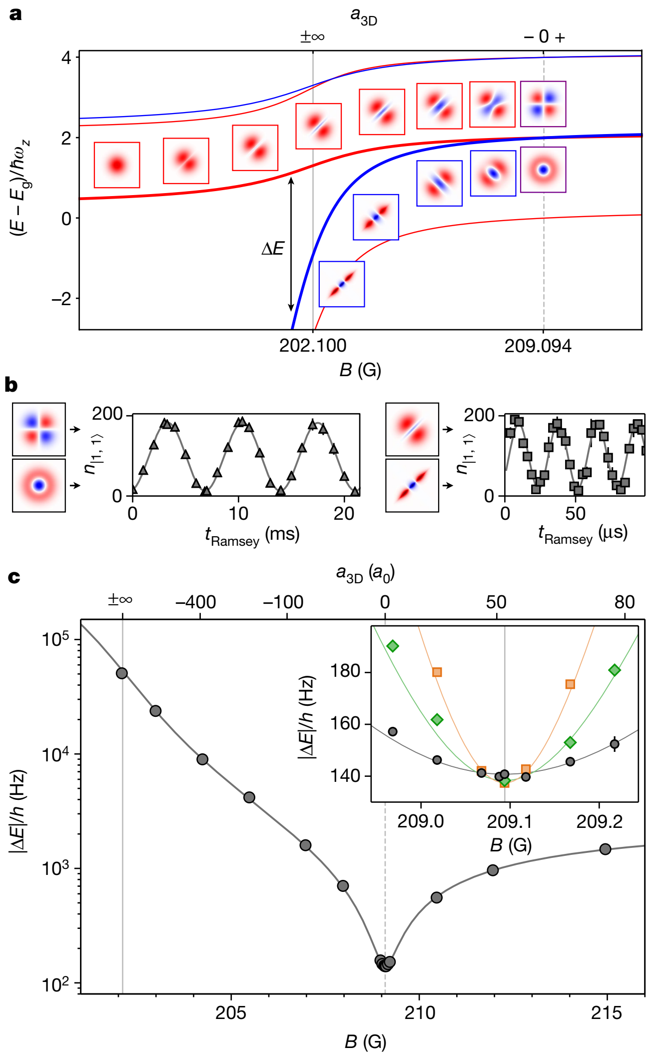

Fig. 3 | Crossover from fermion pair to molecule qubit. a, Theoretical energy spectrum of an interacting fermion pair in the crossover to a molecular state. Pairs in the ground (second excited) COM state are shown in red (blue), with the qubit states highlighted (thick lines). The insets show the approximate 1D pair qubit wavefunctions $\Psi(z_1, z_2)$ with a small trap anharmonicity. Energies E are calculated for an anisotropic 3D harmonic trap with $\omega_x = \omega_y = 3.853\omega_z$ (ref. [31]; Methods). $E_{\rm g}$ is the energy of the non-interacting ground state. **b**, Ramsey interferometry measures the fermion pair qubit energy splitting, ranging from $|\Delta E| = h \times 140.76(3)$ Hz at vanishing interactions (left panel) to $|\Delta E| = h \times 36.00(3)$ kHz near the strongest explored interactions (right panel, $B \approx 202.5$ G). **c**, Measured energy splitting versus magnetic field, from vanishing to strongly attractive and repulsive interactions. The solid line is the theoretical prediction, using the measured recoil gap as an input, without fit parameters. The inset shows the energy splitting at the recoil gap, demonstrating insensitivity to doubling the harmonic frequency from $\omega_z/2\pi = 25.09(4)$ kHz (black) and $\omega_z/2\pi = 38.50(1)$ kHz (green) to $\omega_z/2\pi = 51.8(1)$ kHz (orange). The error bars for $|\Delta E|$ represent sinusoidal fitting error, and are smaller than the datapoints in the main figure.

We now demonstrate that the fermion pair qubit can coherently crossover into the molecular regime[26] of tightly bound fermion pairs. This enables wide tunability of the pair qubit frequency and enables applications for molecular clocks[9,10] and molecule-based quantum information protocols. Figure 3a shows the calculated energy spectrum of the fermion pair in the molecular crossover[30,31]. For every state of COM motion, there is an identical ladder of states of relative motion, starting with the molecular state[34]. The pair qubit states approach degeneracy for vanishing interactions, at the zero of the scattering length $a_{\rm 3D}$ (ref. [35]). There, the approximate 1D two-particle spatial wavefunctions (insets) approach the eigenstates $|1,1\rangle$ and $|0,2\rangle_{\rm s}$ of the recoil gap. For increasing attraction, moving towards the Feshbach resonance, the lower-energy state first evolves into $|2\rangle_{\rm COM}|0\rangle_{\rm rel}$ and then into a deeply bound molecular state with COM motion, with the two atoms therefore strongly bound to each other, as seen by their wavefunction being concentrated near the diagonal $z_1 \approx z_2$. In stark contrast, the higher-energy state evolves into $|0\rangle_{\rm COM}|2\rangle_{\rm rel}$ and then into a strongly repulsive ‘fermionized’ pair[27,29], with largely reduced probability for the two atoms to be at the same location. Near the point of

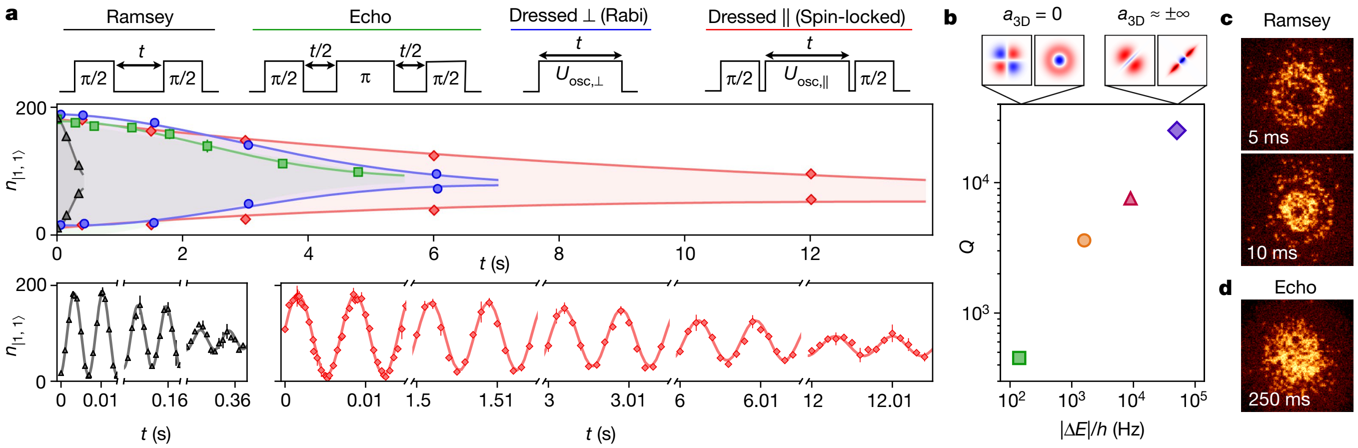

Fig. 4 | Second-scale coherence of the fermion pair qubit. a, A Ramsey oscillation at the recoil gap has a Gaussian envelope (black triangles) with 1/e timescale $\tau = 300(10)$ ms (time series shown below). Inserting an echo π-pulse in a Ramsey oscillation (green squares) extends coherence to $\tau_{\mathrm{Echo}} = 3.2(1)$ s (Gaussian fit), indicating that the phase noise is static. Dressing the pair qubit at the recoil gap with modulated interactions suppresses static noise, extending the coherence time to $\tau = 4.0(3)$ s for a state that is prepared perpendicular to the drive (Rabi oscillation, blue circles, Gaussian fit) and to $\tau = 8.5(5)$ s for a state that is prepared parallel to the drive (spin-locked oscillation, red diamonds, exponential fit). $U_{\mathrm{osc},\perp}$ denotes a Rabi drive with coupling $f_{\mathrm{Rabi}} = 23.902(4)$ Hz, whereas $U_{\mathrm{osc},\parallel}$ denotes the same drive preceded by a quarter period of free evolution (Methods). **b**, The number of coherent oscillations of the fermion pair qubit per decay time, given by the quality factor $Q = |\Delta E|\tau_{\mathrm{Echo}}/h$, grows in the molecular crossover of the fermion pair, from $Q \approx 450$ at vanishing interactions (green square) to $Q \approx 25{,}000$ at $B = 202.091(8)$ G, near the Feshbach resonance (purple diamond, $\tau_{\mathrm{Echo}} = 0.49(2)$ s) (Methods). **c**, Small interaction energy variations owing to the curvature of the lattice beams produce rings in a Ramsey oscillation at $B = 202.091(8)$ G after 10 ms (about 500 oscillations). **d**, A 250-ms echo sequence (about 12,500 oscillations) unwinds these rings to recover spatial coherence. The envelope data in **a**, except for the echo data, are the extreme values of an independent sinusoidal fit over several cycles at each time. The echo data directly obtain the contrast. The shaded regions and decay times τ are extracted from simultaneous fits to all data. The error bars from fit error in **a**, **b** are generally smaller than the datapoints.

fermionization, additional, narrow anharmonicity-mediated resonances exist with molecules in excited transverse COM states[39], where coherent interconversion has been demonstrated[33].

To probe the energy spectrum of the fermion pair qubit, we perform Ramsey interferometry of the register states (Fig. 3b). At vanishing interactions (left panel) anharmonicity interferes with the pair states $|1,1\rangle$ and $|0,2\rangle_S$ at the recoil gap frequency $E_R/h = 140.76(3)$ Hz, with h the Planck constant. In contrast, at strong interactions (right panel) the molecular binding energy drives a much faster Ramsey oscillation at 36.00(3) kHz between a 2D array of strongly repulsive fermion pairs and a lattice of tightly bound molecules[36,40,41]. Ramsey measurements across the Feshbach resonance (Fig. 3c) demonstrate the ability to tune the frequency of the fermion pair qubit, and thus the entangling speed of the motion of fermion pairs, over multiple orders of magnitude.

A key feature of the recoil gap is suppressed sensitivity to laser intensity noise. The inset of Fig. 3c shows the energy gap near zero interactions at different lattice depths. As the trap depth is increased fourfold, the harmonic energy $\hbar\omega_z$ doubles, whereas the recoil gap energy changes by only 2.40(6)%. Moving away from the avoided crossing, the energy difference begins to be determined by interactions. In this regime, increasing the trapping depth confines the atomic wavefunction more tightly and enhances interactions, thus enabling local manipulation of the pair qubit frequency with targeted laser beams[11].

Finally, we explore the coherence of the fermion pair qubit, beginning in Fig. 4a with the properties of the recoil gap states. The decay envelope of various experimental sequences (upper schematics) provides insight into existing noise sources, guiding methods to improve coherence. As a first measurement, we perform a Ramsey experiment that detects intrinsic phase noise. The superposition decays in $\tau = 300(10)$ ms after 40 recoil oscillations, with random spatial structure. In contrast, if an echo π pulse is inserted into the Ramsey oscillation to cancel static noise, coherence is extended to $\tau_{\mathrm{Echo}} = 3.2(1)$ s, corresponding to 450 recoil oscillations and 10^5 harmonic oscillator periods. In combination, these observations indicate the presence of a near-static spatial variation of recoil gap energies on the order of approximatley 0.75 Hz, or 0.5% E_R, within the 2D array.

We eliminate the effects of static noise at the recoil gap by modulating interactions at the recoil gap frequency. This dressing scheme preserves the quantum information in an arbitrary qubit state for over 4 s. The method is analogous to applying an oscillating transverse magnetic field to stabilize an ensemble of dephasing spins[42]. In the frame rotating with the drive, the applied static field is perpendicular to and much larger than any residual dephasing fields, leading to a uniform quantization energy across the ensemble, thereby preserving arbitrary state superpositions. Here, interaction dressing extends coherence to $\tau = 4.0(3)$ s for a state prepared perpendicular to the drive, corresponding to a Rabi oscillation. If the pair qubit is instead first rotated to align with the drive, in spin-locked operation, a further extension of coherence to $\tau = 8.5(5)$ s is observed, and oscillations are still visible after 12 s with good signal to noise. As expected for this driven operation[42], which increases the coherence from the dephasing time T_2 to the population decay time T_1, these decoherence rates approach the natural limits provided by the measured bit-flip rates and loss rates for the two pair qubit states (Methods).

To characterize the coherence of the fermion pair qubit in the molecular crossover, we measure the quality factor $Q = |\Delta E|\tau_{\mathrm{Echo}}/h$ as a function of interaction strength and thus of the fermion pair qubit energy splitting $|\Delta E|$ (Fig. 4b). Remarkably, near the scattering resonance, a superposition of a repulsive fermion pair and a tightly bound molecule remains coherent for 25,000 Ramsey oscillations. The dominant source of decoherence at strong interactions is the underlying curvature of the optical lattice beams, which leads to a radial variation of the local well depth, and a corresponding reduction of the interaction energy by about 0.2% at 10 sites from the centre of the array. This can be observed as spatial rings in a Ramsey experiment near the Feshbach resonance, as in Fig. 4c, taken after 500 oscillations. With an echo pulse (Fig. 4d), these rings refocus spatially even after 12,500 oscillations.

In summary, we have demonstrated a quantum register based on fermion pairs in a 2D optical lattice. Our method provides a route towards quantum simulation and computation by leveraging Pauli exclusion for high-fidelity preparation and control of spin- and motionally entangled states of fermions. Local control of fermion pairs can be achieved using optical tweezers[11,43] to alter the confinement or change the anharmonicity on a lattice site. Alternatively, localized Raman lasers allow for rapid (about 1 μs (ref. [44])) variation of the interaction strength. Shorter-wavelength lattices and lighter mass fermions[18] will allow increasing the speed of the recoil gate by over two orders of magnitude.

Extensions to full gate-based control of entangled many-body states may be realized via locally induced cold collisions[14,45–49], or Rydberg excitation[12,13,50] of pairs[51]; however, these advances will require precise positional control and pristine stability of optical potentials, and mitigation of loss from Rydberg states[52]. Allowing for tunnelling between adjacent sites enables the exploration of extended Fermi–Hubbard models with additional orbital degrees of freedom[53–55]. Furthermore, the accurate simultaneous control of hundreds of molecules in superposition with free atom pairs allows for site-resolved detection of many-body states of dipolar molecules[56], for tests of fundamental symmetries[57,58], and metrology based on molecular clocks[9,10].

Online content

Any methods, additional references, Nature Research reporting summaries, source data, extended data, supplementary information, acknowledgements, peer review information; details of author contributions and competing interests; and statements of data and code availability are available at https://doi.org/10.1038/s41586-021-04205-8.

1. Ludlow, A. D., Boyd, M. M., Ye, J., Peik, E. & Schmidt, P. O. Optical atomic clocks. *Rev. Mod. Phys.* **87**, 637–701 (2015).
2. Xu, V. et al. Probing gravity by holding atoms for 20 seconds. *Science* **366**, 745–749 (2019).
3. Jaksch, D., Briegel, H.-J., Cirac, J. I., Gardiner, C. W. & Zoller, P. Entanglement of atoms via cold controlled collisions. *Phys. Rev. Lett.* **82**, 1975–1978 (1999).
4. Duan, L.-M., Lukin, M. D., Cirac, J. I. & Zoller, P. Long-distance quantum communication with atomic ensembles and linear optics. *Nature* **414**, 413–418 (2001).
5. Islam, R. et al. Measuring entanglement entropy in a quantum many-body system. *Nature* **528**, 77–83 (2015).
6. Bergschneider, A. et al. Experimental characterization of two-particle entanglement through position and momentum correlations. *Nat. Phys.* **15**, 640–644 (2019).
7. Greiner, M., Regal, C. A., Stewart, J. T. & Jin, D. S. Probing pair-correlated fermionic atoms through correlations in atom shot noise. *Phys. Rev. Lett.* **94**, 110401 (2005).
8. Gross, C. & Bakr, W. S. Quantum gas microscopy for single atom and spin detection. *Nat. Phys.* **17**, 1316–1323 (2021).
9. Schiller, S., Bakalov, D. & Korobov, V. I. Simplest molecules as candidates for precise optical clocks. *Phys. Rev. Lett.* **113**, 023004 (2014).
10. Kondov, S. S. et al. Molecular lattice clock with long vibrational coherence. *Nat. Phys.* **15**, 1118–1122 (2019).
11. Weitenberg, C. et al. Single-spin addressing in an atomic Mott insulator. *Nature* **471**, 319–324 (2011).
12. Hollerith, S. et al. Quantum gas microscopy of Rydberg macrodimers. *Science* **364**, 664–667 (2019).
13. Browaeys, A. & Lahaye, T. Many-body physics with individually controlled Rydberg atoms. *Nat. Phys.* **16**, 132–142 (2020).
14. Mamaev, M., Thywissen, J. H. & Rey, A. M. Quantum computation toolbox for decoherence-free qubits using multi-band alkali atoms. *Adv. Quantum Technol.* **3**, 1900132 (2020).
15. Bauer, B., Bravyi, S., Motta, M. & Kin-Lic Chan, G. Quantum algorithms for quantum chemistry and quantum materials science. *Chem. Rev.* **120**, 12685–12717 (2020).
16. Viverit, L., Menotti, C., Calarco, T. & Smerzi, A. Efficient and robust initialization of a qubit register with fermionic atoms. *Phys. Rev. Lett.* **93**, 110401 (2004).
17. Serwane, F. et al. Deterministic preparation of a tunable few-fermion system. *Science* **332**, 336–338 (2011).
18. Chiu, C. S., Ji, G., Mazurenko, A., Greif, D. & Greiner, M. Quantum state engineering of a Hubbard system with ultracold fermions. *Phys. Rev. Lett.* **120**, 243201 (2018).
19. Myrskog, S. H., Fox, J. K., Mitchell, M. W. & Steinberg, A. M. Quantum process tomography on vibrational states of atoms in an optical lattice. *Phys. Rev. A* **72**, 013615 (2005).
20. Müller, T., Fölling, S., Widera, A. & Bloch, I. State preparation and dynamics of ultracold atoms in higher lattice orbitals. *Phys. Rev. Lett.* **99**, 200405 (2007).
21. Förster, L. et al. Microwave control of atomic motion in optical lattices. *Phys. Rev. Lett.* **103**, 233001 (2009).
22. Bakr, W. S. et al. Orbital excitation blockade and algorithmic cooling in quantum gases. *Nature* **480**, 500–503 (2011).
23. van Frank, S. et al. Interferometry with non-classical motional states of a Bose–Einstein condensate. *Nat. Commun.* **5**, 4009 (2014).
24. Kwiat, P. G., Berglund, A. J., Altepeter, J. B. & White, A. G. Experimental verification of decoherence-free subspaces. *Science* **290**, 498–501 (2000).
25. Kielpinski, D. et al. A decoherence-free quantum memory using trapped ions. *Science* **291**, 1013–1015 (2001).
26. Chin, C., Grimm, R., Julienne, P. & Tiesinga, E. Feshbach resonances in ultracold gases. *Rev. Mod. Phys.* **82**, 1225–1286 (2010).
27. Köhl, M., Moritz, H., Stöferle, T., Günter, K. & Esslinger, T. Fermionic atoms in a three dimensional optical lattice: observing Fermi surfaces, dynamics, and interactions. *Phys. Rev. Lett.* **94**, 080403 (2005).
28. Diener, R. B. & Ho, T.-L. Fermions in optical lattices swept across Feshbach resonances. *Phys. Rev. Lett.* **96**, 010402 (2006).
29. Zürn, G. et al. Fermionization of two distinguishable fermions. *Phys. Rev. Lett.* **108**, 075303 (2012).
30. Busch, T., Englert, B.-G., Rzażewski, K. & Wilkens, M. Two cold atoms in a harmonic trap. *Found. Phys.* **28**, 549–559 (1998).
31. Idziaszek, Z. & Calarco, T. Two atoms in an anisotropic harmonic trap. *Phys. Rev. A* **71**, 050701 (2005).
32. Bolda, E., Tiesinga, E. & Julienne, P. Ultracold dimer association induced by a far-off-resonance optical lattice. *Phys. Rev. A* **71**, 033404 (2005).
33. Sala, S. et al. Coherent molecule formation in anharmonic potentials near confinement-induced resonances. *Phys. Rev. Lett.* **110**, 203202 (2013).
34. Sala, S. & Saenz, A. Theory of inelastic confinement-induced resonances due to the coupling of center-of-mass and relative motion. *Phys. Rev. A* **94**, 022713 (2016).
35. Ishmukhamedov, I. S. & Melezhik, V. S. Tunneling of two bosonic atoms from a one-dimensional anharmonic trap. *Phys. Rev. A* **95**, 062701 (2017).
36. Thompson, S. T., Hodby, E. & Wieman, C. E. Ultracold molecule production via a resonant oscillating magnetic field. *Phys. Rev. Lett.* **95**, 190404 (2005).
37. Hartke, T., Oreg, B., Jia, N. & Zwierlein, M. Doublon–hole correlations and fluctuation thermometry in a Fermi–Hubbard gas. *Phys. Rev. Lett.* **125**, 113601 (2020).
38. Fuchs, G. D., Dobrovitski, V. V., Toyli, D. M., Heremans, F. J. & Awschalom, D. D. Gigahertz dynamics of a strongly driven single quantum spin. *Science* **326**, 1520–1522 (2009).
39. Haller, E. et al. Confinement-induced resonances in low-dimensional quantum systems. *Phys. Rev. Lett.* **104**, 153203 (2010).
40. Donley, E. A., Claussen, N. R., Thompson, S. T. & Wieman, C. E. Atom–molecule coherence in a Bose–Einstein condensate. *Nature* **417**, 529–533 (2002).
41. Syassen, N. et al. Atom–molecule Rabi oscillations in a Mott insulator. *Phys. Rev. Lett.* **99**, 033201 (2007).
42. Hartmann, S. R. & Hahn, E. L. Nuclear double resonance in the rotating frame. *Phys. Rev.* **128**, 2042–2053 (1962).
43. Liu, L. R. et al. Molecular assembly of ground-state cooled single atoms. *Phys. Rev. X* **9**, 021039 (2019).
44. Levine, H. et al. Parallel implementation of high-fidelity multiqubit gates with neutral atoms. *Phys. Rev. Lett.* **123**, 170503 (2019).
45. Mandel, O. et al. Controlled collisions for multi-particle entanglement of optically trapped atoms. *Nature* **425**, 937–940 (2003).
46. Anderlini, M. et al. Controlled exchange interaction between pairs of neutral atoms in an optical lattice. *Nature* **448**, 452–456 (2007).
47. Trotzky, S. et al. Time-resolved observation and control of superexchange interactions with ultracold atoms in optical lattices. *Science* **319**, 295–299 (2008).
48. Greif, D., Uehlinger, T., Jotzu, G., Tarruell, L. & Esslinger, T. Short-range quantum magnetism of ultracold fermions in an optical lattice. *Science* **340**, 1307–1310 (2013).
49. Kaufman, A. M. et al. Entangling two transportable neutral atoms via local spin exchange. *Nature* **527**, 208–211 (2015).
50. Rom, T. et al. State selective production of molecules in optical lattices. *Phys. Rev. Lett.* **93**, 073002 (2004).
51. Greene, C. H., Dickinson, A. S. & Sadeghpour, H. R. Creation of polar and nonpolar ultra-long-range Rydberg molecules. *Phys. Rev. Lett.* **85**, 2458–2461 (2000).
52. Guardado-Sanchez, E. et al. Quench dynamics of a Fermi gas with strong nonlocal interactions. *Phys. Rev. X* **11**, 021036 (2021).
53. Ho, A. F. Fermions in optical lattices near a Feshbach resonance: from band insulator to Mott insulator. *Phys. Rev. A* **73**, 061601 (2006).
54. Koga, A., Kawakami, N., Rice, T. M. & Sigrist, M. Orbital-selective Mott transitions in the degenerate Hubbard model. *Phys. Rev. Lett.* **92**, 216402 (2004).
55. Kubo, K. Pairing symmetry in a two-orbital Hubbard model on a square lattice. *Phys. Rev. B* **75**, 224509 (2007).
56. Yan, B. et al. Observation of dipolar spin-exchange interactions with lattice-confined polar molecules. *Nature* **501**, 521–525 (2013).
57. Baron, J. et al. Order of magnitude smaller limit on the electric dipole moment of the electron. *Science* **343**, 269–272 (2014).
58. Cairncross, W. B. et al. Precision measurement of the electron's electric dipole moment using trapped molecular ions. *Phys. Rev. Lett.* **119**, 153001 (2017).

Methods

Experimental setup

Fermion pair qubits are composed of atoms in the two lowest hyperfine states of ^{40}K: $|F=9/2, m_F=-9/2\rangle$ and $|F=9/2, m_F=-7/2\rangle$, with F the hyperfine quantum number and m_F the magnetic quantum number. These states have an approximately 7-G-wide s-wave Feshbach resonance at $B_\infty \approx 202.1$ G and a zero crossing of interactions at $B_0 = 209.094(8)$ G (measured). The spatial potential experienced by each atom is formed by two 1,064-nm lattice beams reflecting off a superpolished substrate forming the first facet of the microscope objective[37,59]. Each beam propagates near-horizontally in either the x or y direction (Fig. 1a), with a shallow angle of incidence to the x–y plane of about 10.2°, and is polarized in the x–y plane. The two beams reflect off the (horizontal) substrate of the quantum gas microscope at this angle to form a long wavelength lattice in the z direction ($a_z \approx 3$ μm), before being directly retro-reflected to form a short wavelength lattice in the x and y directions ($a_x \approx a_y \approx 541$ nm). The net potential in the z direction on each lattice site is the sum of the two potentials formed by the two lattice beams. After initialization, the potential is kept sufficiently deep to prevent all tunnelling between sites on relevant timescales.

In a typical experiment, atoms are prepared near 151 G at repulsive interactions. To initialize fermion pairs in the qubit subspace, the magnetic field is ramped across the Feshbach resonance to 208 G in about 80 ms, which is sufficiently fast to avoid narrow resonances between fermion pairs and molecules in higher COM states, either in transverse[33] or z-directional motion, that all occur at fields below about 202 G (ref. [31]). A further field ramp to zero interactions at 209.094 G, in another aprroximately 100 ms, initializes fermion pairs in the state $|1, 1\rangle$, the upper of the two recoil eigenstates. At the recoil gap, the measured loss rates for the two pair qubit states $|1, 1\rangle$ and $|0, 2\rangle_s$ are 0.00(2) Hz and 0.08(3) Hz, respectively, and the measured bit-flip rates are 0.06(1) Hz and 0.05(3) Hz, respectively.

To drive Rabi oscillations between $|1, 1\rangle$ and $|0, 2\rangle_s$ at the recoil gap, interactions are modulated from repulsive to attractive at 140.65 Hz using the magnetic field (Fig. 2a). State $|1, 1\rangle$ is converted to $|0, 2\rangle_s$ and vice versa with a probability of 99.9973(3)%, as calculated from the decay of the contrast of Rabi oscillations ($f_{\text{Rabi}} = 23.902(4)$ Hz, $\tau = 4.0(3)$ s, Gaussian fit). Some fermion pairs in excited vibrational states give spurious, but constant, contributions to the signal, reducing oscillation contrast to 92(1)%. A route to improve this contrast through better sample preparation techniques has been demonstrated in recent experiments[18] that achieve low-entropy arrays with fermion pair densities exceeding 99.5%.

For readout, an additional 1,064-nm superlattice that is directly retro-reflected in the z direction (532-nm lattice spacing) coherently separates the long wavelength z lattice into a double well[60], as described in Fig. 2b[37]. This superlattice remains off except during readout. Through this process, only lattice sites with two atoms originally in state $|1, 1\rangle$ appear bright, whereas sites with two atoms initially in $|0, 2\rangle_s$ appear fully dark. Imperfect preparation of pair qubits can lead to some sites that are occupied by fluorescent single atoms. To more easily distinguish state $|1, 1\rangle$ from these single atoms, the applied double well is tilted during the splitting process to move all singly occupied sites into a specific layer, which can then be made dark by tuning the relative fluorescence of the two vertical layers, as demonstrated in previous work[37]. The variable $n_{|1,1\rangle}$ counts the bright sites in a circle of radius ten sites at the centre of the atomic cloud. Repeated images of the same cloud reveal an imaging loss of $n_{|1,1\rangle}$ of about 12%. Improved imaging loss rates near 2% have been demonstrated[61].

Energy spectrum calculation

The energy spectrum of two identical atoms in a 3D anisotropic harmonic trap interacting via a delta function potential can be calculated exactly, given the 3D scattering length and the harmonic trap frequencies[31,62]. The trap frequencies $\omega_x/2\pi = 96.84(4)$ kHz, $\omega_y/2\pi = 96.55(4)$ kHz and $\omega_z/2\pi = 25.09(4)$ kHz are measured via lattice intensity modulation spectroscopy. The 3D scattering length a_{3D} of the lowest two hyperfine states of ^{40}K as a function of magnetic field is provided by a theoretical calculation (private communication with A. Simoni, calculations based on the model in ref. [63]), adjusted for the new precise measurement reported here (Fig. 3c, inset) on the location of the scattering length zero: $B_0 = 209.094(8)$ G. The scattering length is well approximated by the formula $a_{\text{3D}} = a_{\text{bg}}(1-(B_0-B_\infty)/(B-B_\infty))$ with $B_\infty = 202.1$ G and background scattering length $a_{\text{bg}} = 167.6a_0$, where a_0 is the Bohr radius. The mean value of ω_x and ω_y, which differ by less than 0.4%, is used to obtain a trap ratio $\omega_x/\omega_z = \omega_y/\omega_z = 3.853(6)$ for input to the theory for an anisotropic 3D harmonic trap in Fig. 3a[31]. This energy spectrum is also used to calculate the energy difference $|\Delta U/2|$ for display in Fig. 2d. For the theoretical energy difference in Fig. 3c (main panel), the measured recoil gap frequency of 140.76(3) Hz at zero interactions is added as a Rabi coupling to the spectrum of Fig. 3a, likewise for other lattice depths reported in the inset.

Recoil gap calculation

The magnitude of the recoil gap at vanishing interactions in a 1D lattice potential can be derived using perturbation theory. Corrections proportional to z^4 in the potential are included up to second order in perturbation theory, and corrections proportional to z^6 are included to first order in perturbation theory. The resulting energy of vibrational state $|n\rangle$ in a lattice potential $VE_{\text{R}}\sin^2(\pi z/a_z)$ to this order is

$$E_n = 2E_{\text{R}}\sqrt{V}\left(n+\frac{1}{2}\right) - E_{\text{R}}\left(\frac{2n^2+2n+1}{4}\right) - E_{\text{R}}\frac{1}{\sqrt{V}}\left(\frac{2n^3+3n^2+3n+1}{16}\right). \tag{1}$$

The recoil gap between the pair states $|1, 1\rangle$ and $|0, 2\rangle_s$ is

$$2E_1 - (E_2 + E_0) = E_{\text{R}}\left(1 + \frac{9}{8\sqrt{V}}\right). \tag{2}$$

The exact energies can be obtained from solutions to Mathieu's equation[64].

Interacting energy gap calculation

The two atoms interact via a delta function potential $\hat{U} = (4\pi\hbar^2 a_{\text{3D}}/m)\,\delta^{(3)}(\mathbf{r}_1 - \mathbf{r}_2)$ (refs. [30,31]). The first-order perturbative energy shift $\langle\hat{U}\rangle$ for a given state is more easily evaluated in the basis of suitably normalized COM and relative coordinates, $\mathbf{R} \equiv (\mathbf{r}_1 + \mathbf{r}_2)/\sqrt{2}$ and $\mathbf{r} \equiv (\mathbf{r}_1 - \mathbf{r}_2)/\sqrt{2}$, respectively.

We first calculate $\langle\hat{U}\rangle$ for the ground state. At vanishing interactions, in the absence of anharmonicity, the ground state of the trap is the harmonic oscillator ground state in x, y and z for both atoms

$$\Psi(\mathbf{r}_1, \mathbf{r}_2) = \prod_{\mu\in\{1,2\},\ i\in\{x,y,z\}} \frac{e^{-(r_{\mu,i}/l_i)^2/2}}{(\pi l_i^2)^{\frac{1}{4}}}, \tag{3}$$

where $l_i = \sqrt{\hbar/m\omega_i}$ is the harmonic oscillator length for coordinate $r_{\mu,i}$ of atom μ in direction i. To evaluate $\langle\hat{U}\rangle$, one can transform to $\mathbf{R}$ and $\mathbf{r}$ coordinates. The form of the wavefunction is identical

$$\Psi(\mathbf{R}, \mathbf{r}) = \prod_{i\in\{x,y,z\}} \frac{e^{-(R_i/l_i)^2/2}}{(\pi l_i^2)^{\frac{1}{4}}} \frac{e^{-(r_i/l_i)^2/2}}{(\pi l_i^2)^{\frac{1}{4}}}, \tag{4}$$

and the form of $\hat{U}$ is $(4\pi\hbar^2 a_{\text{3D}}/m)(\delta^{(3)}(\mathbf{r})/2^{3/2})$. The operator $\hat{U}$ does not affect the coordinate $\mathbf{R}$, and the wavefunctions of $\mathbf{R}$ are already normalized. Thus, the ground-state energy shift at weak interactions is

$$U \equiv \langle \hat{U} \rangle = \frac{4\pi\hbar^2 a_{3D}}{m}\frac{1}{2^{3/2}}\frac{1}{\pi^{3/2} l_x l_y l_z}. \tag{5}$$

In a quasi-1D geometry, the transverse wavefunction (that is, for motion along x and y) remains in the harmonic ground state for weak interactions. One can then work in the basis of normalized harmonic oscillator states of the rotated z coordinates, $z_c = (z_1 + z_2)/\sqrt{2}$ and $z_r = (z_1 - z_2)/\sqrt{2}$, with the understanding that the transverse state is the ground state. The two pair qubit states can be written as $|2\rangle_{\mathrm{COM}}|0\rangle_{\mathrm{rel}} = (|0,2\rangle_s + |1,1\rangle)/\sqrt{2}$ and $|0\rangle_{\mathrm{COM}}|2\rangle_{\mathrm{rel}} = (|0,2\rangle_s - |1,1\rangle)/\sqrt{2}$. The interaction energy shift depends solely on the magnitude of the relative wavefunction at $z_r = 0$, which is a factor of $\sqrt{2}$ smaller in state $|2\rangle_{\mathrm{rel}}$ than in state $|0\rangle_{\mathrm{rel}}$. Thus, the energy shift is $U/2$ for $|0\rangle_{\mathrm{COM}}|2\rangle_{\mathrm{rel}}$, whereas it is U for $|2\rangle_{\mathrm{COM}}|0\rangle_{\mathrm{rel}}$.

Qubit control protocols

Extended Data Fig. 1 describes in more detail the experimental methods used to control the fermion pair qubit by tuning the interaction strength via the magnetic field.

To achieve population transfer between $|1,1\rangle$ and $|0,2\rangle_s$ (Fig. 2 data), pairs are initialized at the recoil gap. Aside from an overall offset, the static effective Hamiltonian near the recoil gap is

$$H = \frac{E_R}{2}\sigma_z + \frac{U}{4}\sigma_x \tag{6}$$

in the basis ($|1,1\rangle$, $|0,2\rangle_s$), where σ_z and σ_x are the Pauli matrices. A Rabi oscillation is driven (Extended Data Fig. 1a) by modulating the interaction energy U by ΔU about vanishing interactions at the recoil gap frequency

$$H(t) = \frac{E_R}{2}\sigma_z + \frac{\Delta U}{4}\sin(E_R t/\hbar)\sigma_x. \tag{7}$$

This Hamiltonian is produced by sinusoidal modulation of the magnetic field in time t, $B(t) = B_0 + \Delta B \sin(E_R t/\hbar)$, with $B_0 = 209.094$ G being the field where the interactions vanish. The resulting frequency of Rabi oscillation is $f_{\mathrm{Rabi}} = \Delta U/4h$. Each drive operation begins as a sine wave, and the applied amplitude ΔB is varied to achieve a π/2 pulse (left panel of Extended Data Fig. 1a, $f_{\mathrm{Rabi}} = E_R/12h$, $\Delta B_{\pi/2} \approx 50$ mG) or π pulse (right panel of Extended Data Fig. 1a, $f_{\mathrm{Rabi}} = E_R/6h$, $\Delta B_{\pi} \approx 100$ mG) in exactly 3 drive cycles.

In a Ramsey measurement (Fig. 3 data), a π/2 pulse creates a superposition of $|1,1\rangle$ and $|0,2\rangle_s$, the two states acquire a relative phase due to their energy difference, and a π/2 pulse re-interferes the superposition (Extended Data Fig. 1b, upper panel). A Ramsey measurement at finite interactions proceeds analogously, with the addition of magnetic field ramps to and from a test field B_R (lower panel). The ramps between B_0 and B_R are adiabatic and have a fixed shape and timing. They thus prepare a precise superposition at field B_R with a fixed initial relative phase. Varying the intermediate hold time t_{Ramsey} at B_R then drives additional relative phase accumulation, determined only by the qubit energy splitting at B_R, which is detected via re-interference.

Protocols for measuring coherence (Fig. 4 data) are shown in Extended Data Fig. 1c. A π pulse is added to the midpoint of the Ramsey protocol to perform an echo sequence (upper panel). Echo coherence measurements at finite interactions proceed identically, with two additional sets of field ramps to allow phase evolution at a desired field. In the ⊥ dressed state protocol (lower left panel), a Rabi drive is continually applied at the π-pulse amplitude. In the || dressed state protocol (lower right panel), a π/2 pulse is followed by a delay by a quarter of the recoil gap period, sinusoidal dressing and a final π/2 pulse. Viewed in the frame rotating with the drive, each pulse provides a static quantization on the Bloch sphere of states $|1,1\rangle$ and $|0,2\rangle_s$. The first π/2 pulse is along the x axis, and rotates the state from the z axis to the y axis. The $h/4E_R$ delay then leaves the state unchanged, but ensures that the subsequent applied dressing is along the y axis, aligned with the state vector. The final π/2 pulse lies in the x–y plane of the rotating frame. The orientation of this pulse rotates with the dressing time, leading to oscillation.

Strong driving

Extended Data Fig. 2 shows the fermion pair qubit dynamics under strong driving, with a Rabi coupling comparable to the energy splitting of the effective two-level system. The observed multiple frequencies in the response are analogous to the transition frequencies between eigenstates of a two-level atom dressed by light at strong driving. Initializing a specific state where the atom and field are not coupled prepares a superposition of more than two eigenstates of the strongly coupled system, leading to multifrequency interference[65,66].

Coherence at strong interactions

An echo sequence (see schematic in Fig. 4a) measures the decay of fermion pair qubit coherence at strong interactions (Extended Data Fig. 3). For each repeated experiment at a fixed total time t_{Echo}, a random extra phase from 0 to 2π is added to the fermion pair qubit by redistributing evolution time before and after the echo π pulse. The standard deviation of the signal $n_{|1,1\rangle}$ then decays owing to loss of coherence within the register array, from which the coherence time is obtained, shown in Fig. 4b.

Data availability

The data that support the findings of this study are available from the corresponding authors upon reasonable request. Source data are provided with this paper.

59. Cheuk, L. W. et al. Quantum-gas microscope for fermionic atoms. *Phys. Rev. Lett.* **114**, 193001 (2015).
60. Murmann, S. et al. Two fermions in a double well: exploring a fundamental building block of the Hubbard model. *Phys. Rev. Lett.* **114**, 080402 (2015).
61. Mitra, D. et al. Quantum gas microscopy of an attractive Fermi–Hubbard system. *Nat. Phys.* **14**, 173–177 (2018).
62. Chen, Y., Xiao, D.-W., Zhang, R. & Zhang, P. Analytical solution for the spectrum of two ultracold atoms in a completely anisotropic confinement. *Phys. Rev. A* **101**, 053624 (2020).
63. D'Errico, C. et al. Feshbach resonances in ultracold 39K. *New J. Phys.* **9**, 223–223 (2007).
64. Daniel, D. J. Exact solutions of Mathieu's equation. *Prog. Theor. Exp. Phys.* **2020**, 043A01 (2020).
65. Laucht, A. et al. Breaking the rotating wave approximation for a strongly driven dressed single-electron spin. *Phys. Rev. B* **94**, 161302 (2016).
66. Wang, G., Liu, Y.-X. & Cappellaro, P. Observation of the high-order Mollow triplet by quantum mode control with concatenated continuous driving. *Phys. Rev. A* **103**, 022415 (2021).

Acknowledgements We thank C. Robens for discussions. This work was supported by the NSF through the Center for Ultracold Atoms and Grant PHY-2012110, ONR (grant number N00014-17-1-2257), AFOSR (grant number FA9550-16-1-0324), AFOSR-MURIs on Quantum Phases of Matter (grant number FA9550-14-1-0035) and on Full Quantum State Control at Single Molecule Levels (grant number FA9550-21-1-0069), the Gordon and Betty Moore Foundation through grant GBMF5279, and the Vannevar Bush Faculty Fellowship. M.Z. acknowledges support from the Alexander von Humboldt Foundation.

Author contributions The experiment was designed by all authors. T.H., B.O. and N.J. collected and analysed the data. All authors contributed to the manuscript.

Competing interests The authors declare no competing interests.

Additional information

Supplementary information The online version contains supplementary material available at https://doi.org/10.1038/s41586-021-04205-8.

Correspondence and requests for materials should be addressed to Thomas Hartke or Martin Zwierlein.

Peer review information *Nature* thanks the anonymous reviewers for their contribution to the peer review of this work.

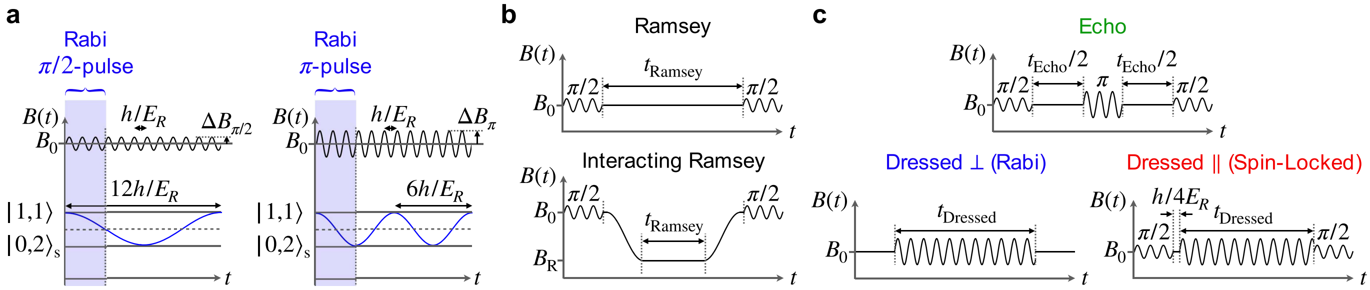

Extended Data Fig. 1 | Qubit control protocols. **a**, Protocol to transfer population between the fermion pair qubit eigenstates at the recoil gap via a Rabi drive of interactions using the magnetic field (Fig. 2 data). **b**, Protocols for Ramsey measurements of the qubit energy splitting $|\Delta E|$ (Fig. 3 data). **c**, Protocols for measuring coherence at the recoil gap (Fig. 4 data).

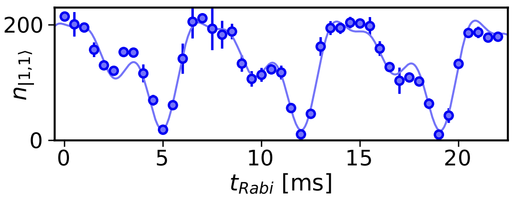

Extended Data Fig. 2 | Strong driving. A strongly driven Rabi oscillation at the avoided crossing of Fig. 1c exhibits non-sinusoidal response. The predicted Rabi coupling $\Delta U/4 = h \times 151.98$ Hz (see Fig. 2d), which is driven at a modulation frequency of 140.65 Hz, is comparable to the recoil energy gap $E_R = h \times 140.76(3)$ Hz. The solid line shows a phenomenological guide to the eye composed of three sinusoids with frequencies near E_R/h, $2E_R/h$ and $3E_R/h$.

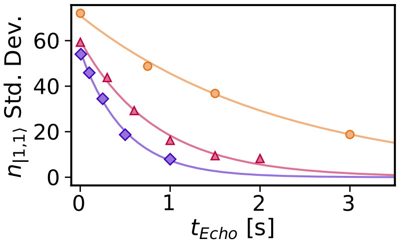

Extended Data Fig. 3 | Coherence at strong interactions. The standard deviation of the fermion pair qubit state in an echo sequence with randomized extra phase (standard deviation of $n_{|1,1\rangle}$) quantifies the coherence of the register array at strong interactions. A fitted exponential without offset has 1/*e* time constant $\tau = 2.3(1)$ s at $|\Delta E| = h \times 1.594(7)$ kHz (orange), $\tau = 0.84(5)$ s at $|\Delta E| = h \times 8.98(7)$ kHz (red) and $\tau = 0.49(2)$ s at $|\Delta E| = h \times 50.7(4)$ kHz (purple), corresponding to magnetic fields $B = 206.976(8)$ G, $B = 204.235(8)$ G and $B = 202.091(8)$ G, respectively. Error bars of τ represent fit error. These data are used in Fig. 4b.